Journal of
Manufacturing and Materials Processing

MDPI

Article

Precision Calibration in Wire-Arc-Directed Energy Deposition Simulations Using a Machine-Learning-Based Multi-Fidelity Model

Fuad Hasan, Abderrachid Hamrani *, Md Munim Rayhan, Tyler Dolmetsch, Dwayne McDaniel and Arvind Agarwal

Department of Mechanical and Materials Engineering, Florida International University, Miami, FL 33199, USA; fhasa011@fiu.edu (F.H.); mrayhan@fiu.edu (M.M.R.); tdolmets@fiu.edu (T.D.); mcdaniel@fiu.edu (D.M.); agarwala@fiu.edu (A.A.)
* Correspondence: ahamrani@fiu.edu

Abstract: Thermal simulation is essential in wire-arc-directed energy deposition (W-DED) to accurately estimate temperature distributions, impacting residual stress and distortion in components. Proper calibration of simulation models minimizes inaccuracies caused by varying material properties, machine settings, and environmental conditions. The lack of standardized calibration methods further complicates thermal predictions. This paper introduces a novel calibration method integrating both machine learning, as the high-fidelity (HF) model, and response surface modeling, as the low-fidelity (LF) model, within a multi-fidelity (MF) framework. The approach utilizes Bayesian optimization to effectively explore the search space for optimal solutions. A two-tiered model employs the LF model to identify feasible regions, followed by the HF model to refine calibration parameters, such as thermal efficiency (η), convection coefficient (h), and emissivity (ε), which are difficult to determine experimentally. A three-factor Box–Behnken design (BBD) is applied to explore the design space, requiring only thirteen parameter configurations, conserving resources and enabling robust model training. The efficacy of this MF model is demonstrated in multi-layer W-DED calibration, showing strong alignment between experimental and simulated temperatures, with a mean absolute error (MAE) of 7.47 °C. This method offers a replicable framework for broader additive manufacturing processes.

Keywords: additive manufacturing; wire-arc-directed energy deposition (W-DED); thermal simulation; calibration methods; machine learning; multi-fidelity modeling

Citation: Hasan, F.; Hamrani, A.; Rayhan, M.M.; Dolmetsch, T.; McDaniel, D.; Agarwal, A. Precision Calibration in Wire-Arc-Directed Energy Deposition Simulations Using a Machine-Learning-Based Multi-Fidelity Model. *J. Manuf. Mater. Process.* **2024**, *8*, 222. https://doi.org/10.3390/jmmp8050222

Academic Editors: Alireza Vahedi Nemani, Mahya Ghaffari and Ali M. Nasiri

Received: 5 September 2024
Revised: 28 September 2024
Accepted: 30 September 2024
Published: 2 October 2024

1. Introduction

Additive manufacturing (AM) has revolutionized the manufacturing landscape by offering unparalleled flexibility in producing complex geometries with a wide range of materials. Among the various AM techniques, wire-arc-directed energy deposition (W-DED), also known as wire-arc additive manufacturing (WAAM), has emerged as a promising method for producing large metal components due to its fast deposition rate, particularly benefiting the aerospace, automotive, and marine industries [1,2]. W-DED employs an electric arc as the heat source to melt metal wire, which is deposited layer-by-layer to build a part. This process is cost-effective for large-scale fabrications and is also well-suited for repair and remanufacturing applications [3]. Despite its significant advantages, challenges are faced in the W-DED process, particularly in controlling thermal processes that significantly impact the microstructure, mechanical properties, and dimensional accuracy of the manufactured parts. The inherent complexity of thermal management in W-DED arises from the need to balance heat input to ensure good adhesion between layers while minimizing distortions and residual stresses [4,5].

Thermal analysis using finite element modeling (FEM) has been extensively applied to understand and optimize the W-DED process across various critical areas of application. For instance, process parameters, such as heat input, travel speed, and material feed rate, could be fine-tuned using FEM thermal analysis, which is crucial for ensuring the structural integrity and mechanical properties of fabricated parts [6,7]. Additionally, FEM can be used to predict and mitigate residual stresses and distortions caused by differential cooling rates across deposited layers [8,9]. Moreover, thermal simulations play a crucial role in the development of effective deposition strategies. Optimal tool paths that minimize thermal gradients and ensure uniform layer deposition are determined, which is particularly critical when dealing with complex geometries and overhanging structures [10,11].

However, the effectiveness of these simulations critically depends on the accurate calibration of the model. Accurate calibration of simulations involves replicating the experimental setup and estimating heat source parameters, including the effective power used in welding. While physical entities, such as geometry size, bead geometry, layer count, bead height and width, and temperature measurement locations, can be directly measured or estimated, obtaining parameters such as the thermal efficiency factor (η), convection film coefficient (h), and emissivity (ε) presents significant challenges. These parameters are difficult to measure accurately and are subject to variability due to changes in materials, machine settings, and environmental conditions [12–15]. Traditionally, these critical parameters are manually adjusted through an iterative trial-and-error process based on empirical estimates. For instance, Zhao et al. and Yang et al. have both demonstrated iterative calibration of η, h, and ε, adjusting these parameters through trial-and-error until their simulation models aligned with experimental outcomes [16,17]. This traditional approach, foundational yet inflexible, demands extensive recalibrations when experimental conditions vary, consuming considerable time and computational resources [18–20]. Such challenges highlight the need for more efficient and systematic calibration techniques. To address these challenges, the application of advanced modeling techniques can significantly streamline the calibration process. These techniques have already shown promise in various areas, such as process modeling, optimization, and process monitoring, particularly within W-DED [21–25]. However, efforts to standardize the calibration of thermal analysis in W-DED are still lacking. Recent work by Strobl. et al., employing a proper generalized decomposition (PGD) model for estimating parameters in WAAM simulations, represents a promising starting point [26]. While this approach helps to bypass some of the computational burdens typical of FEM in the initial phase, it also introduces its own computational complexities early in the process. Additionally, the calibration is primarily validated for single-layer applications, which may limit its utility for multi-layer depositions without further adjustments. In the broader field of AM, initiatives to calibrate uncertain parameters in the melt pool, address deformations caused by residual stresses, and to develop meta-models for predicting melt pool dimensions under specific configurations have been undertaken [27–30]. Yet, there remains a notable gap in directly validating simulation models against experimental temperature distributions.

To bridge the gap between simulation and actual process outcomes in W-DED, this study aims to develop and validate a novel calibration method that incorporates a machine-learning-based multi-fidelity (MF) model. Recognizing the inherent limitations of current calibration practices, marked by computationally intensive procedures and high susceptibility to errors, our study focuses on integrating advanced computational tools to enhance the simulation accuracy and reduce resource consumption. The objective is to design a dynamic calibration framework that can adapt to varying operational conditions and material properties, thus providing a reliable basis for predicting thermal behavior in W-DED processes. By leveraging a combination of low- and high-fidelity models within a Bayesian optimization framework, we aim to establish a robust calibration protocol that improves the predictive capabilities of thermal simulations, as well as substantiate its effectiveness through comprehensive experimental validation.

The study is structured to systematically outline the developed methodology, starting with a discussion on FEM to establish the foundational understanding of thermal phenomena in W-DED processes in Section 2. This section also introduces the calibration approach, detailing critical parameter selection and a design of experiments (DOE) approach. It further explores the integration of low-fidelity (LF) and high-fidelity (HF) models, culminating in a calibration model using Bayesian optimization. Section 3 presents the results and discussions through a comprehensive case study, beginning with a detailed account of how experimental data were acquired to calibrate the simulation model. Details of the simulation model and parameters are included, and the details of the DOE and MF surrogate model are discussed, along with the calibration results. Finally, Section 4 discusses the conclusion and future work, providing insights into the implications of the findings and outlining potential avenues for further research.

2. Methodology

In this section, we outline the procedural framework and computational techniques utilized to simulate the thermal dynamics of W-DED processes through FEM. A detailed exposition of the model setup, incorporating a description of the geometric and material properties essential for the simulation, is provided. The implementation of the heat transfer equations and the specifics of heat source modeling, which were pivotal for understanding the temperature distribution within the material, is explored. Additionally, the boundary conditions set for the simulations and the use of the element birth and death technique to model material deposition are outlined. Furthermore, the MF modeling approach is introduced, integrating both low-fidelity and high-fidelity models to enhance the calibration and accuracy of our simulations.

2.1. Finite Element Modeling for W-DED Thermal Analysis

A systematic workflow of the simulation process for W-DED thermal analysis is illustrated in Figure 1.

To begin the FEM simulation, a 3D CAD model was needed that encompasses both the substrate and the deposited geometry. The model accounts for the material properties, which vary with temperature, such as density, thermal conductivity, and specific heat capacity. The next step involved discretizing the spatial domain into small elements, modeling the heat source, and applying proper initial and boundary conditions. Finally, the deposition strategy was planned, specifying path planning, layer thickness, width, number of layers, and dwell time.

These components were integrated within a FEM software environment (Ansys R2 (22.2)), executing a numerical simulation that yielded the temperature field, T. The field varied with time, t, and spatial coordinates (x, y, z) and was governed by the 3D nonlinear heat transfer equation, expressed as follows [31]:

$$\frac{\partial}{\partial x}\left(k\frac{\partial T}{\partial x}\right)+\frac{\partial}{\partial y}\left(k\frac{\partial T}{\partial y}\right)+\frac{\partial}{\partial z}\left(k\frac{\partial T}{\partial z}\right)+q=\frac{\partial\left(\rho C_p T\right)}{\partial t}, \quad (1)$$

where, k is the conductivity, C_p is the specific heat, ρ is the material density, and q is the volumetric heat source.

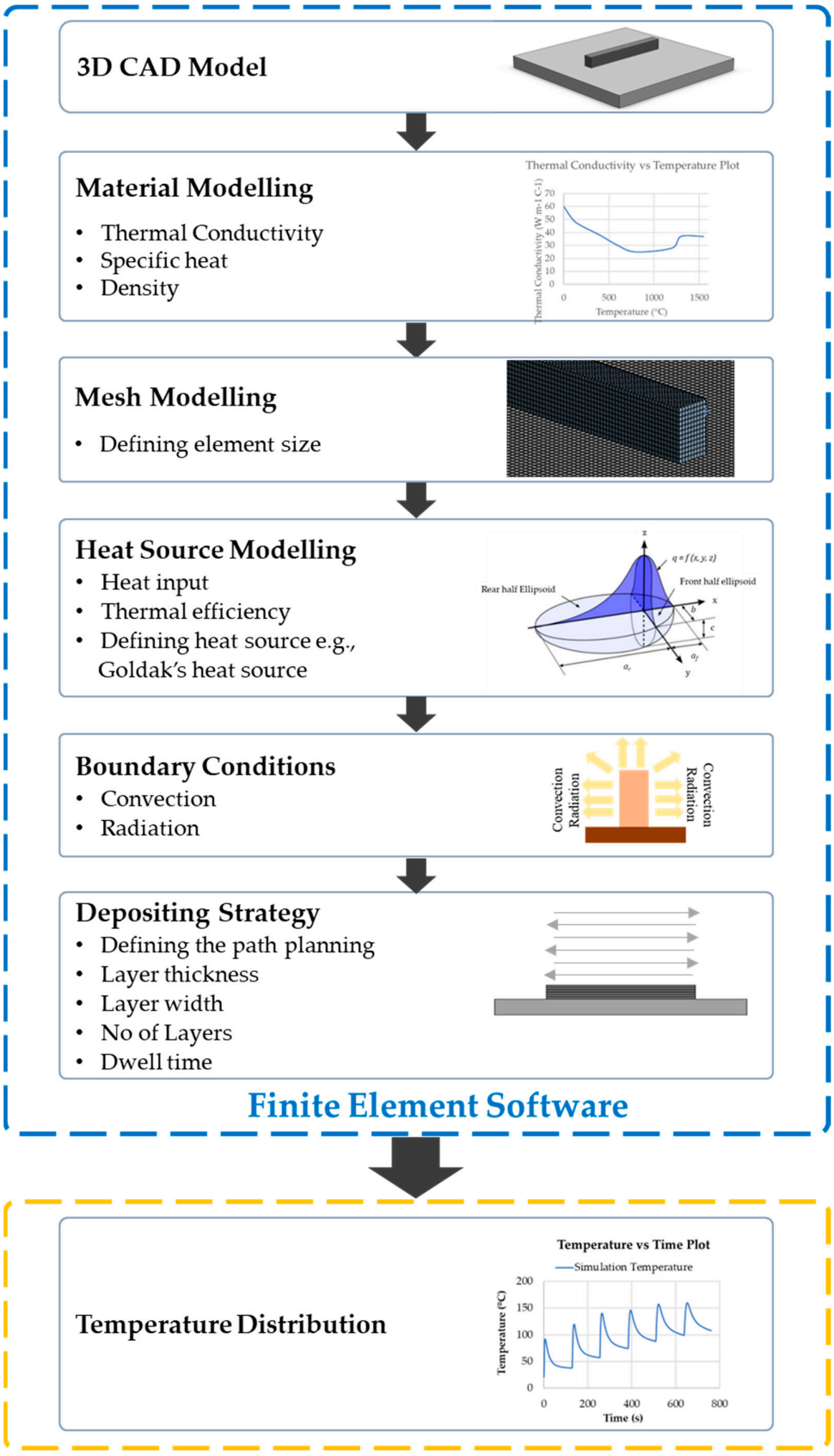

Figure 1. Schematic of the FEM process for W-DED thermal analysis.

2.1.1. Heat Source Modeling

Heat source modeling was utilized in the simulation of W-DED to precisely simulate the complex thermal interactions inherent in the material deposition process. This aspect of modeling was crucial, as it facilitates an accurate depiction of the heat's impact on both the substrate and the deposited material.

Through the integration of heat source models, such as the Goldak double-ellipsoidal model (Figure 2) [32], simulations were enabled to predict temperature gradients and stress distributions more effectively. In this study, the Goldak double-ellipsoidal heat source was utilized, represented by the following equations:

$$q_f(x,y,z) = \frac{6\sqrt{3qf_f}}{a_f bc\pi\sqrt{\pi}} e^{\left(-\frac{3x^2}{a_f^2}-\frac{3y^2}{b^2}-\frac{3z^2}{c^2}\right)}, \text{ for } x \geq 0 \quad (2)$$

$$q_r(x,y,z) = \frac{6\sqrt{3qf_r}}{a_r bc\pi\sqrt{\pi}} e^{\left(-\frac{3x^2}{a_r^2}-\frac{3y^2}{b^2}-\frac{3z^2}{c^2}\right)}, \text{ for } x < 0 \quad (3)$$

where, q_f and q_r are the heat flux on the front and rear semi-ellipsoids, respectively, a_f is the length of the front ellipsoidal semi-axes, and a_r is the length of the rear ellipsoidal semi-axes. The parameter b represents the width of the heat source, while c indicates its depth. The factors f_f and f_r are responsible for determining the heat distribution in the front and rear halves of the heat source, respectively, and $f_f + f_r = 2$. In this context, the variable q represents the energy input while considering η, calculated as per the equation provided:

$$Q = \eta \times q, \quad (4)$$

where, η is the thermal efficiency factor, which ranges from 0 to 1.

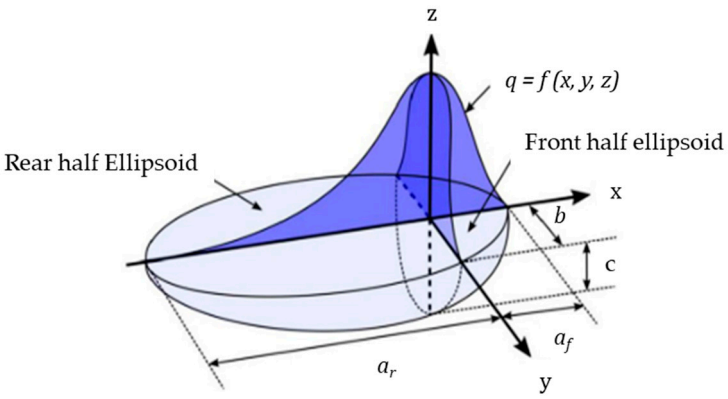

Figure 2. Schematic representation of Goldak's double-ellipsoidal heat source model [33].

2.1.2. Boundary Conditions

To accurately simulate the thermal environment of the W-DED process, specific boundary conditions were defined. The initial temperatures of the materials were established at ambient levels. Throughout the thermal analysis, the effects of convection and radiation between the surface and the surrounding environment were considered and modeled using the following equations:

$$q_{conv} = h_\infty (T_\infty - T), \text{ and } q_{rad} = \varepsilon \sigma ({T_\infty}^4 - T^4), \quad (5)$$

where, h_∞ is the convection coefficient, T_∞ is the ambient temperature, ε is the emissivity, and σ is the Stefan–Boltzmann constant, given as 5.67×10^{-8} Wm^{-2} K^{-4} [34].

2.1.3. Material Deposition

To simulate the sequential addition of material in the W-DED process, the element birth and death technique was employed [35]. This technique allowed for the activation (birth) and deactivation (death) of elements to replicate the physical process of material deposition and the corresponding thermal history (Figure 3).

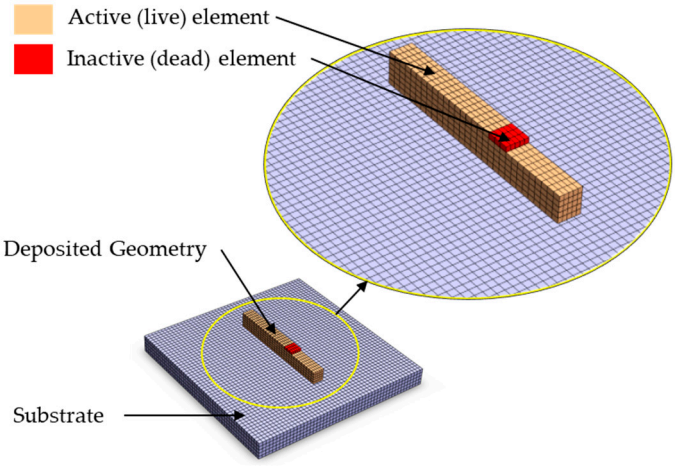

Figure 3. Illustration of element birth and death adopted in the FEM model.

This mirrored the physical addition of material and the corresponding thermal effects in W-DED, ensuring that only the elements representing currently deposited layers contributed to the thermal calculations. Also, this study emphasized temperature distribution during the deposition and, as such, the shape and size of the deposition geometry, illustrated as a cuboid, were designed to suffice for thermal analysis and did not impact the focal thermal behavior evaluations.

The accuracy of FEM simulations relied heavily on precise input parameters, mainly derived from experiments. However, measuring certain parameters, such as η, h, and ε, was challenging due to their complex nature. These parameters were vital for simulations to accurately mirror reality, yet direct measurement was often difficult. Consequently, a robust calibration procedure became essential to iteratively adjust these parameters within the simulation framework, ensuring the modeled outcomes were reflective of the physical reality of the W-DED process.

2.2. Calibration Process

Achieving high-fidelity prediction of temperature distribution in W-DED simulations was inherently challenging due to the assumptions required during model development. This complexity was further amplified by the difficulty of directly measuring certain critical parameters that significantly influence thermal predictions. Among these, the thermal efficiency, convection film coefficient, and emissivity were crucial for the accuracy of W-DED processes. These parameters were selected due to their direct impact on the heat transfer dynamics within the material and because of the complexity of measuring them in the experimental phase: thermal efficiency determined the amount of input power converted to heat, the convection film coefficient affected heat dissipation to the environment, and emissivity influenced radiative heat loss. Notably, they cannot be adjusted through other direct or indirect factors that are easily measurable. However, other parameters could also play significant roles, such as thermal conductivity (k; affected how quickly heat spread through the material), specific heat capacity (c; influenced the material's ability to store heat), and density (ρ; affected the material's thermal inertia and how it responded to heating). These parameters (i.e., k, c, and ρ) were not selected for the initial focus due to the relative ease of obtaining their values from existing material property databases and their comparatively less variable nature under typical process conditions. The calibration process

was characterized by a multi-step methodology that began with the creation of a plan using the DOE technique for executing numerous simulation models under varying settings.

This initial phase was crucial for establishing the foundation for further modeling efforts. Subsequently, a response surface model (RSM), the low-fidelity model, was constructed based on the data derived from the DOE. The LF collaborated with a machine learning (ML) model, the high-fidelity model, to predict the target values and ascertain the most effective settings. The primary objective was to align the simulation results with actual experimental data and to identify the optimal settings. These parameters were then employed in the simulation model to derive the temperature distribution generated by the simulation, which served for the validation of the model to confirm its accuracy and reliability in determining the optimal parameters. An illustration of the MF calibration process of the W-DED simulations is presented in Figure 4.

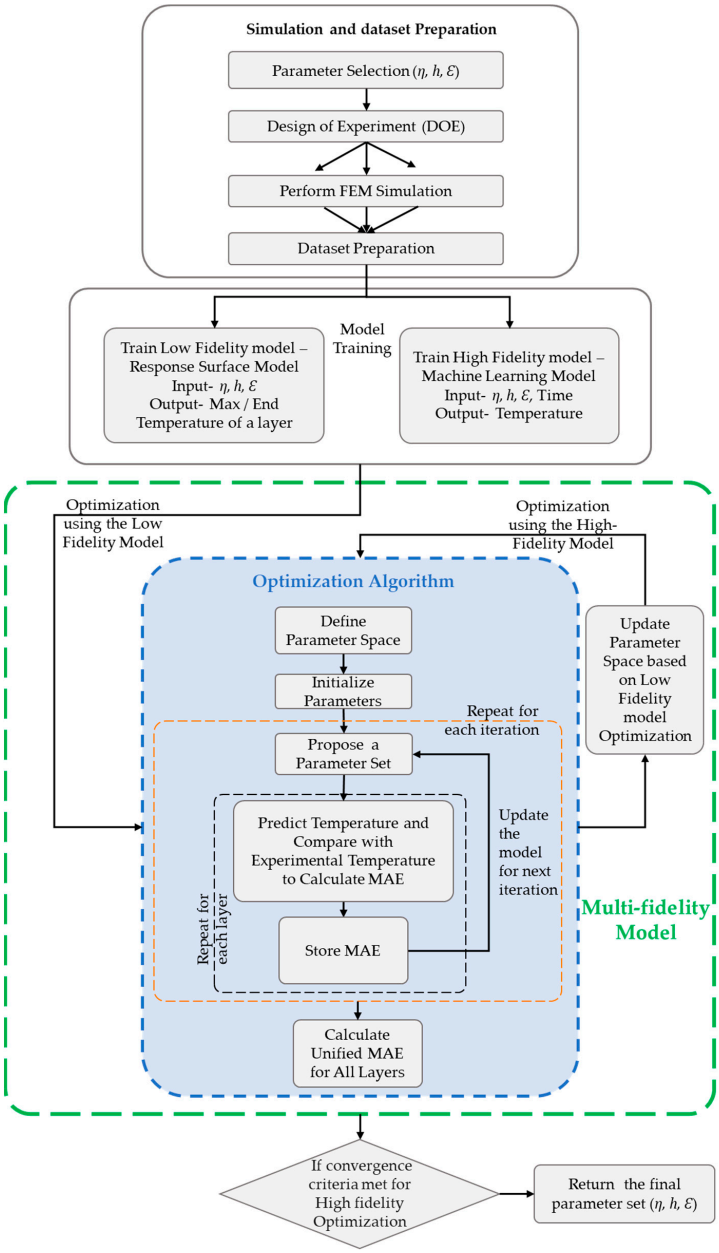

Figure 4. Flowchart representation of the MF calibration process in W-DED thermal analysis.

2.2.1. Design of Experiments Strategy

To systematically explore the parameter space, a DOE approach was implemented in our study. Among the various DOE methodologies available, the three-factor Box–Behnken design (BBD) [36] was selected for its notable efficiency in navigating experimental space with a reduced number of simulations (Figure 5). This choice was driven by the need to balance the depth of the parameter exploration with practical considerations, such as resource limitations and time constraints. The BBD was particularly advantageous for this study due to its ability to provide sufficient data for the development of a robust model without the extensive number of runs compared to a full factorial design (FFD) or the potential edge-of-range issues associated with the central composite design (CCD).

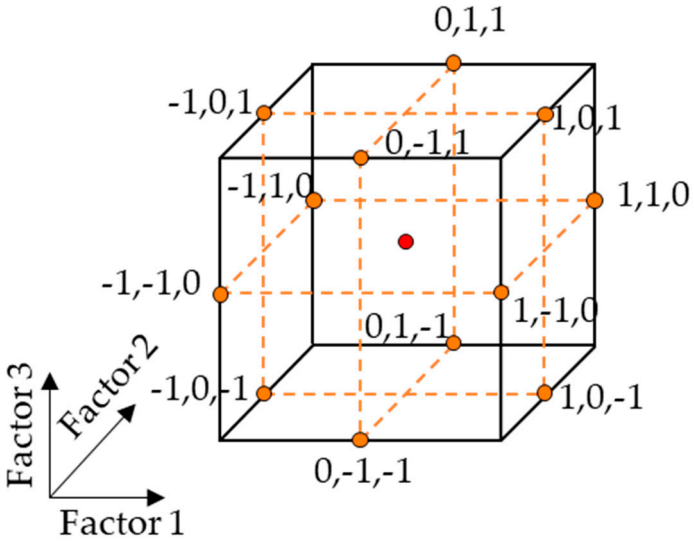

Figure 5. Representation of the Box–Behnken design with three factors.

2.2.2. Multi-Fidelity Approach

The calibration of our simulation model of the W-DED process employed a MF strategy, integrating both LF and HF models to refine parameters and enhance the accuracy of simulations. Initially, the LF model, which demanded less computational effort, was deployed to broadly assess the impact of various settings, effectively narrowing the scope for parameter exploration. Following this, the HF model, which was more computationally intensive, was utilized to provide an accurate representation of the simulation dynamics. Insights derived from the LF model guided the focused application of the HF model, ensuring efficient parameter optimization. Furthermore, the MF model acted as a surrogate to the more computationally demanding FEM, striking a balance between computational efficiency and accuracy. This approach was particularly advantageous for performing inverse analysis, which involved extracting realistic simulation parameters from the observed data. By combining the MF model with an optimization technique, the calibration process was significantly improved. This combination allowed for the systematic adjustment of simulation parameters based on performance metrics, thereby improving the simulation's ability to replicate actual physical phenomena accurately. Moreover, this methodology reduced the computational load and accelerated the identification of optimal parameters.

Low-Fidelity Model

In the early phase of calibrating the W-DED simulation, a RSM was used based on the radial basis function (RBF) interpolator with a thin-plate spline kernel as the LF model. This kernel was particularly suited for our purposes, as it provided a balance between flexibility and smoothness in interpolation. RBF was perfect for the initial stages because it could rapidly evaluate the simulation parameters while using minimal computing power. The LF model was trained using data from the set of simulations prescribed by the DOE

strategy that explored different combinations of key parameters, including η, h, and ε. This dataset (D_{LFM}) captured the maximum temperature (T_{max}) and the temperature at the end of the dwell time (T_{end}) for each deposited layer and will be available in the Supplementary Data (Figure 6).

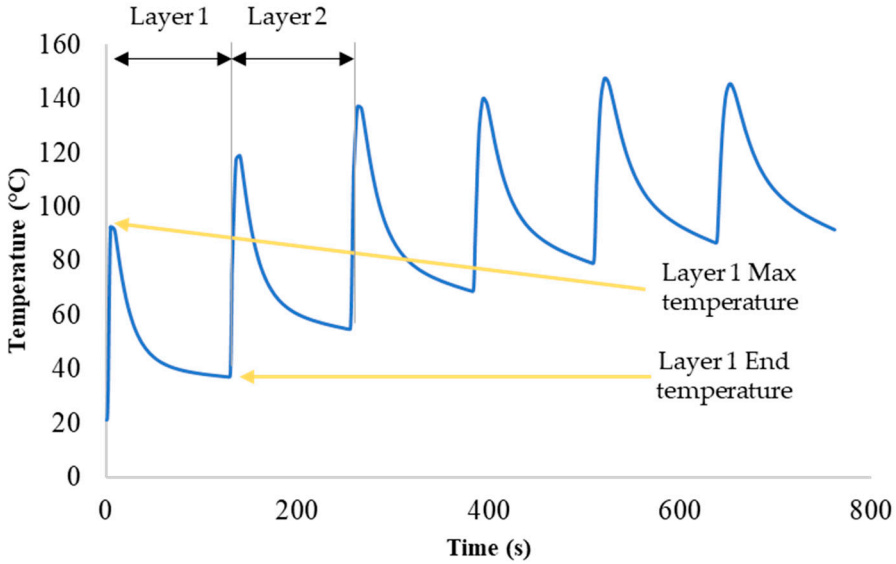

Figure 6. Typical temperature profile versus time plot for thin-wall W-DED deposition.

By focusing on these critical temperature points, the thermal characteristics of the deposition process could be effectively assessed without becoming overwhelmed by excessive detail. The first step in the calibration process was to gather and organize the data for each deposited layer. The data were represented as a set of parameters and their corresponding temperatures, as follows: $\{(\eta_i, h_i, \varepsilon_i), T_i\}$ for $i = 1, 2, \ldots, n$. In this notation, $(\eta_i, h_i, \varepsilon_i)$ stands for the ith combination of η, h, and ε, and T_i is the temperature associated with that specific parameter combination. The variable n represents the total number of parameter combinations being tested, which was determined by our DOE strategy.

The value of this radial function in the RBF model was determined by the distance from a central point within the parameter space, enabling spatially aware interpolation.

For coefficient calculation, the weights, λ_i, were calculated by the model such that the interpolator, $s(x)$, at an input point, $x = (\eta, h, \varepsilon)$, is given by [37]:

$$s(x) = \sum_{i=1}^{n} \lambda_i \phi(\| x - x_i \|) + p(x), \quad (6)$$

where, $x_i = (\eta_i, h_i, \varepsilon_i)$ are the known parameter points from the dataset, ϕ is the RBF corresponding to the thin-plate spline kernel, $p(x)$ is an additional polynomial term incorporated to achieve uniqueness and control extrapolation behavior, and $\|x - x_i\|$ denotes the Euclidean distance. Optimization was key for the λ_i coefficients, ensuring that the RBF interpolator closely fit the data points. This typically involved resolving a linear system formulated from the parameter space distances [38,39]. Once the λ_i coefficients were optimized, the RBF model was prepared to forecast temperatures for parameter sets that had not yet been explored. The model, utilizing RBFs centered on the known points, x_i, and the derived weights, λ_i, interpolated the temperature for any new input, x. The RBF model benefited from radial symmetry, enabling a smooth transition of the temperature response across the parameter space, effectively mimicking the thermal dynamics of the W-DED process. This interpolation process was inherently efficient and served as an essential step to refine the parameter space in the calibration procedure.

High-Fidelity Model

The HF model in our calibration process leveraged ML to predict the temperature profiles at each data point with precision. This model utilized a DOE simulation-based dataset (D_{HFM}) that included key variables, i.e., η, h, and ε, as well as the time (t), and this dataset will be available in the Supplementary Data. Unlike the LF model, which takes in specific data points (T_{max} and T_{end}) for each layer, the HF model processes a continuous stream of temperature data at every timestep throughout the deposition process. The extensive temporal data (t) allow the HF model to utilize the complete temperature distribution for different simulation runs, capturing the complete heating and cooling behavior in the W-DED process.

The regression task in ML was formulated typically, as follows: Given a set of input features, X (i.e., W-DED simulation parameters: η, h, ε, and t), the goal was to predict a continuous output, y, which in our case was the temperature (T). The model learned a function, $f(X)$, during the training phase, which was then used to make predictions on new, unseen data. The regression model was represented by the equation:

$$y = f(X) + \xi, \tag{7}$$

where, $f(X)$ is the function learned from the data during the training phase, and ξ is the error term representing the noise in the data.

An extensive analysis was conducted on a range of ten ML regression models to determine the most effective one for predicting temperature. Among the various models evaluated, one model was selected as superior, excelling in predictive accuracy, computational efficiency, and its ability to generalize across different datasets. A detailed discussion on the selected model and its comparative analysis against others is provided in the Results Section.

2.2.3. Optimization

The optimization stage within our calibration framework employed the Gaussian process (GP)-based Bayesian optimization to efficiently and effectively determine the optimal parameters for W-DED process simulation. The core of the optimization was represented by the objective function, $g(x)$, where $x = (\eta, h, \varepsilon)$ symbolizes the vector of design parameters adopted for the calibration. The objective was to minimize the mean absolute error (MAE) between the predictions from the MF surrogate model and the experimental temperature values across different layers, expressed as:

$$Minimize\ MAE = \frac{1}{n}\sum_{i=1}^{n}\left|T_{exp,i} - g(x_i; \eta,\ h,\ \varepsilon)\right|, \tag{8}$$

where, T_{exp},i is the experimental temperature at the ith data point, g (x_i; η, h, ε) is the temperature prediction from the GP model based on the design parameters, and x_i represents the set of parameters at the ith evaluation.

The GP served as a probabilistic surrogate to approximate the function $g(x)$, employing the Matérn covariance function to ensure smooth variations in MAE in response to minor changes in the parameters (η, h, and ε) [40,41]. The optimization process was guided by the expected improvement (EI) acquisition function, which aims to maximize the expected reduction in MAE [42]. This function was crucial for identifying potential improvements through adjustments in η, h, and ε based on the observed temperatures. After each function evaluation, Bayesian inference was used to update the GP model, integrating new data to refine MAE predictions. This update highlighted the impact of each parameter on the observed temperatures. After each evaluation of the objective function, the GP model was updated using Bayesian inference, integrating new data to refine the MAE predictions. This update accounted for the impact of each parameter, i.e., η, h, and ε, on the observed temperatures.

In summary, each cycle of the optimization process iteratively defined the parameter space, assessed the initial viability with the LF model, refined choices with the HF model, and employed Bayesian optimization to converge on optimal parameters, minimizing MAE until no significant gains were observed. To provide a clear and structured overview of the complex interactions and decision points within our optimization framework, the steps were compiled into a pseudo-algorithm. This algorithm illustrated the systematic actions taken to achieve effective calibration of our simulation model. Algorithm 1 presents the sequential steps, detailing each phase from initialization through to the final optimization, encapsulating our methodical approach to enhancing simulation accuracy for W-DED processes.

Algorithm 1: MF Calibration Approach of W-DED Thermal Analysis

Input: Low-fidelity model dataset, D_{LFM}, HF model dataset, D_{HFM}, experimental dataset, D_{exp}
Output: Optimized parameter set Θ^* (η, h, ε)
Initialize LF model M_{LFM} using D_{LFM} with inputs η, h, and ε and outputs T_{max} and T_{end} for each layer
Initialize HF model M_{HFM} using D_{HFM} with inputs η, h, ε, and t and output T at time t
Define design space $X \subseteq \mathbb{R}^n$ for parameters: η, h, and ε
LF Model Optimization:
for each layer in D_{exp} **do**
    Extract layer-specific experimental data for comparison
    Calculate predictions for T_{max} and T_{end} using $M_{LFM}(\theta)$
    Compare predictions with experimental data from D_{exp}
    Calculate MAE for each layer
end for
Calculate unified MAE across all layers
Return optimized parameters from low-fidelity model Θ_{LFM} (η, h, ε)
Update design space based on Θ_{LFM}
HF Model Optimization:
for each layer in D_{exp} **do**
    Extract layer-specific experimental data for detailed comparison
    Calculate predictions for temperature profile T using M_{HFM} (θ) with updated X
    Calculate MAE for all temperature points per layer
end for
Calculate unified layer MAE across all layers
if reduction in MAE < threshold **then**
    Stop optimization and retrieve best parameters Θ^* (η, h, ε)
end if
return optimized parameters Θ^*

3. Results and Discussions

The outcomes and details of the experimental setup, which was designed to ensure the reliability and consistency of the data obtained, are first presented in this section. The specifics of the simulation models are covered, including heat source parameters, meshing techniques, material properties, and a parameter sensitivity analysis. The discussion continues with the presentation of DOE details and results from both the LF and HF models. The section concludes with a discussion on the calibration results, emphasizing the challenges addressed and successes achieved in the calibration of the simulation model using the MF calibration approach.

3.1. Experimental Setup

The experimental setup, the methodology employed for data collection, and the subsequent analysis are detailed in this section, providing a clear linkage between experimental observations and simulation adjustments. To acquire temperature data for the calibration process, a reliable baseline of experimental data was required against which to calibrate our

simulation model. Thin-wall deposition was chosen for its geometric simplicity. Accordingly, a six-layer thin wall was constructed, each layer measuring 64 mm in length, with a 122 s dwell time between layers. This longer dwell time allowed for the comparison across more data points during the cooling period, since the heating or deposition period was relatively short. The W-DED system comprised a Fronius CMT 400i power source coupled with an ABB IRB 2600 robot. For the deposition, φ 1.2 mm copper-coated AWS ER70S-6 wire was used. This wire's composition includes carbon (C) 0.06–0.15%, manganese (Mn) 1.40–1.85%, silicon (Si) 0.80–1.15%, phosphorus (P) 0.025%, sulfur (S) 0.035%, nickel (Ni) 0.15%, chromium (Cr) 0.15%, molybdenum (Mo) 0.15%, and vanadium (V) 0.03%. The wire was deposited onto a substrate (101.6 mm × 101.6 mm × 9.53 mm) of ASTM A36 mild steel material. The process involved a shielding gas mix of 90% Ar and 10% CO_2 at 18 L/min. A visual guide to the setup and a CAD representation of the wall after deposition and the path of the torch are provided in Figure 7.

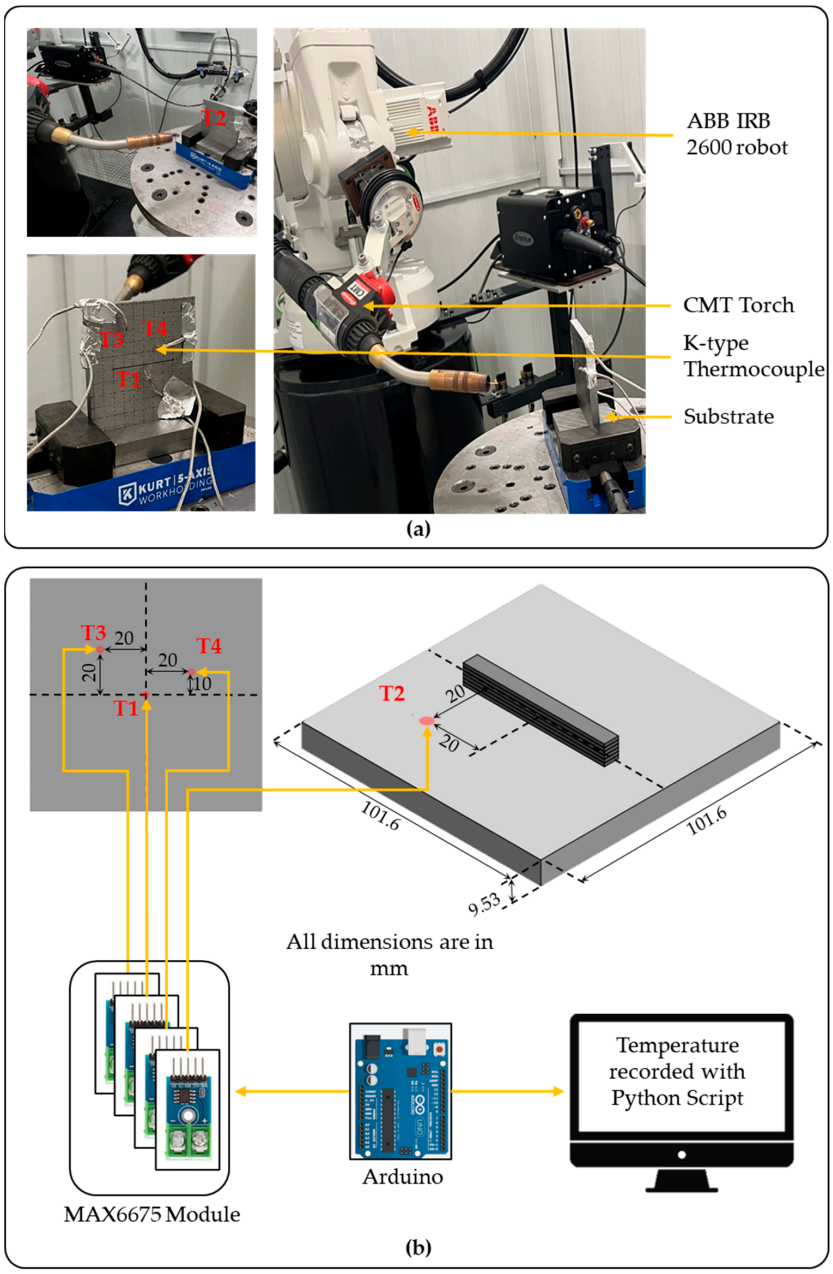

Figure 7. (**a**) Experimental setup. (**b**) Data acquisition process.

Four K-type thermocouples were used with a MAX6675 Module to obtain temperature readings at T1, T2, T3, and T4 locations. T1, T3, and T4 were positioned on the back side of the substrate, while T2 was located on the welding side. All thermocouples were set at a safe distance of at least 10 mm from the center line of the deposition. This arrangement was chosen to protect the thermocouples from heat damage and interference from the deposited material. An Arduino microcontroller was utilized to interface with the thermocouples and acquire temperature data, while temperature logging was performed using a Python script. The thermocouples had a temperature range spanning from 0 to 1024 °C. Direct contact between the thermocouples and the substrate was ensured to maintain accuracy in temperature measurements. Deposition parameters are detailed in Table 1.

Table 1. Deposition parameters during the experiment.

Parameter	Value	Unit
Torch velocity	12.7	mm/s
Wire feed speed	5	m/min
Contact-to-work distance	15	mm

To demonstrate the reliability of our experimental data, the experiment was repeated multiple times. Figure 8 presents a comparative analysis of the temperature-over-time plots at the T4 location across three trials, all of which show strong consistency. In this study, the temperature readings from the T1 and T4 thermocouples were used because these locations were closest to the welding line.

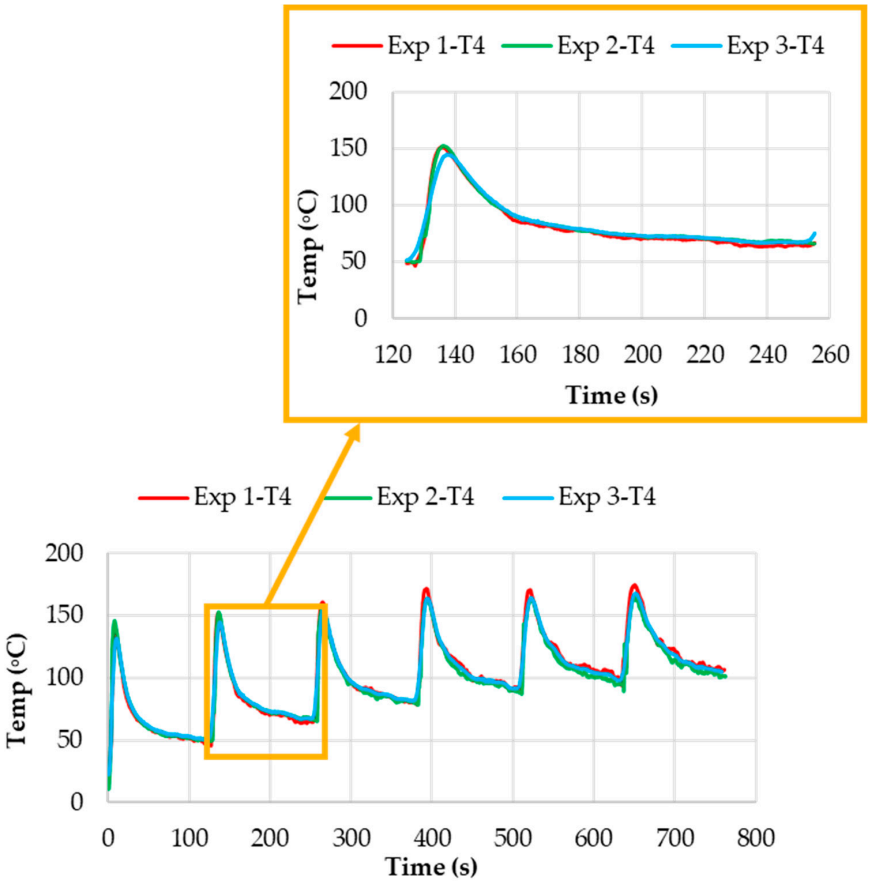

Figure 8. Comparison plot among Exp 1, Exp 2, and Exp 3 at location T4.

3.2. Simulation Setup

3.2.1. Simulation Parameters and Heat Source Configuration

The subsequent phase involved transferring the experimental data into our simulation framework to ensure accurate model inputs. In Table 2, the parameters are categorized as directly available from the experimental setup or as variables that needed to be estimated or derived for simulation purposes. The Ansys APDL script was utilized to input these parameters, which included defining the substrate and deposit dimensions, material information, and process parameters, such as torch velocity, layer thickness, and dwell time. Additionally, the script was configured to incorporate the Goldak heat source parameters and account for cooling times between each layer.

Table 2. Parameters used to model the wire DED process simulation.

Parameters	Experimental Value	Simulation Value
Substrate	101.6 mm × 101.6 mm × 9.53 mm	Same as experimental
Deposit	64 mm × 6 mm × 8.4 mm (average)	Same as experimental
Substrate material	ASTM A36	Same as experimental
Deposited material	ER 70S-6	Same as experimental
Torch velocity	12.7 mm/s	Same as experimental
Layer thickness	6 mm	Same as experimental
No. of layers	6	Same as experimental
Dwell time between layers	122 s	Same as experimental
Mean power	3.32 KW	Same as experimental
η	Not available from experiment	Not available (estimated for simulation)
Effective power (Q = mean power × η)	η × 3.32 KW	Same as experimental
Ambient temperature	21 °C	Same as experimental
Thermocouple location	As specified in Figure 7	Same as experimental
h	Not available from experiment	Not available (estimated for simulation)
ε	Not available from experiment	Not available (estimated for simulation)
Goldak heat source parameter(a_f, a_r, f_f, f_r, b, c)	Listed in Table 3	Same as experimental

Table 3. Heat source parameters adopted in this study.

af (mm)	a_r (mm)	f_f	f_r	b (mm)	c (mm)	Q (W)
6	12	0.6	1.4	3.8	1.2	3320

As highlighted in the methodology, factors such as η, h, and ε were not directly measurable. The machine's nominal input power was set at 3.32 kW, which served as a baseline. However, the actual power absorbed can fluctuate due to variables, such as wire feed speed and arc stability. To manage this, we introduced η (thermal efficiency) as an input parameter in our simulation to model the real power conversion efficiency, acknowledging the variability in power absorption. A value of 1 indicates perfect efficiency (i.e., all the power was absorbed), while lower values represent increasing levels of power loss. In the simulation, heat losses due to convection and radiation can be modeled if h

and ε are available. Typically, these parameters are determined through trial-and-error in conventional calibration approaches, which can be time-consuming and inefficient. In our case, however, the calibration model was used to refine these parameters, enhancing the accuracy and efficiency of our simulations.

To determine the shape parameters of the Goldak heat source (a_f, a_r, f_f, f_r, b, and c), a typical cross-sectional macrograph of the deposited material was analyzed, as shown in Figure 9.

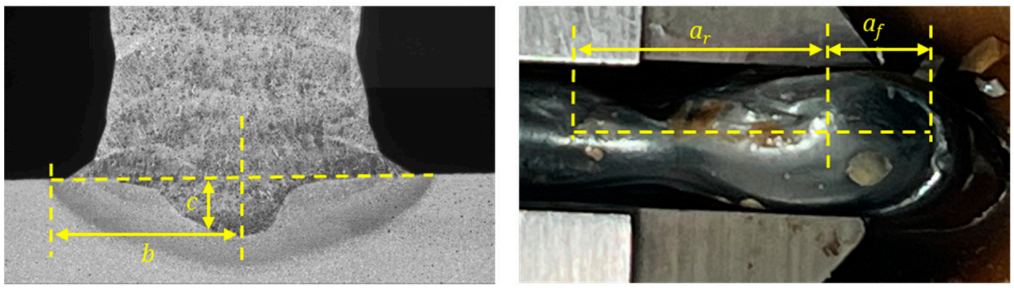

Figure 9. Heat source parameters from the cross-sectional macrographs of the deposited material.

These macrographs revealed the melt pool geometry, which is directly related to the heat source distribution. By measuring the dimensions of the melt pool in the front, rear, width, and depth directions, the corresponding Goldak parameters were estimated. The values of f_f and f_r, where ($f_f + f_r = 2$), were assumed to be 0.6 and 1.4, respectively [43]. Table 3 provides the heat source parameters used in this study.

3.2.2. Mesh Model and Material Properties

The meshing of our simulation model was critical for achieving accurate results. As shown in Figure 10, the model employed an 8-node solid element, termed "brick" in Ansys. The mesh dimensions were set at 1.4 mm × 1.4 mm × 1.2 mm for the substrate, and 1.5 mm × 1.5 mm × 2 mm for the deposited geometry. Overall, the model comprised 30,540 nodes and 24,500 elements, providing a detailed representation to capture the nuances of thermal behavior during the deposition process.

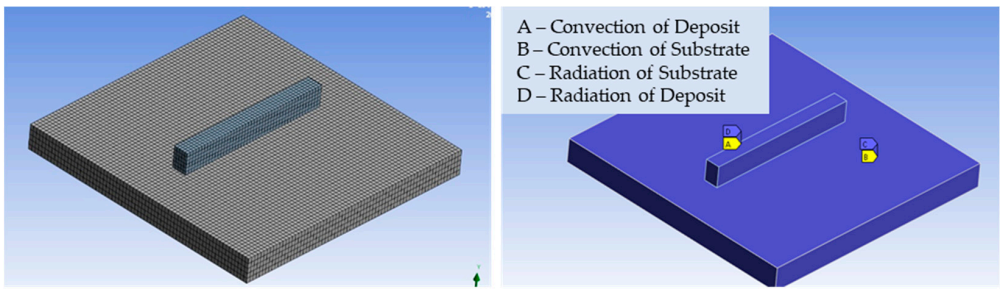

Figure 10. (**a**) Mesh model and (**b**) boundary conditions used in the Ansys simulation.

Regarding material specifics, ASTM A36 and ER70S-6 were used for the substrate and deposited geometry, respectively, mirroring the experimental setup. The properties of these materials were sourced from the literature [32,44].

3.3. Design of Experiment

As outlined in our methodology, the subsequent step involved implementing a DOE to minimize the number of simulations required for effective calibration. To illustrate the number of simulations required by various DOE strategies, Table A1 provides a comparison, highlighting that the BBD required the fewest simulations, making it the most efficient choice for our needs. The design space selected for investigation through the DOE is

presented in Table 4. The ranges for each parameter were carefully chosen based on an extensive review of relevant literature using different materials and machines used in W-DED processes [32,45–55]. This ensured that the ranges were representative of realistic operational conditions for the W-DED process.

Table 4. Ranges of simulation parameters derived from the literature.

Parameters	Minimum Value	Maximum Value
η	0.6	0.99
h (W/mm^2)	0.000005	0.00005
ε	0.01	0.99

The three-level configurations used in our BBD are detailed in Table A2. The BBD facilitated the exploration of the simulation parameter space without the need for an excessive number of simulations. In addition, a parameter sensitivity analysis was conducted within this range of parameters to demonstrate how each parameter affected the temperature profile during the heating and cooling periods. Details of this analysis can be found in Figure A1 of Appendix A.

3.4. Multi-Fidelity Surrogate Model

3.4.1. Low-Fidelity Model

For each layer of deposition, two distinct LF models were constructed: one for predicting the T_{max} during the deposition and another for estimating T_{end}. Various interpolation models were compared to enhance the accuracy of these predictions (Table A3 in Appendix B). The comparison included linear, polynomial, RBF, and kriging models. Among these, the RBF model consistently outperformed the others, achieving an R^2 of 1 and an MSE close to 0 for both T_{max} and T_{end}. This superior performance highlights the effectiveness of the RBF model in capturing the thermal dynamics during the material deposition process. Graphical presentations of the RBF-LF model predictions for T_{max} and T_{end} across all layers are provided in Figures A2 and A3 of Appendix B. Also, a comparison of T_{max} and T_{end} between RBF prediction and experimental data at location T1 is shown in Figure 11.

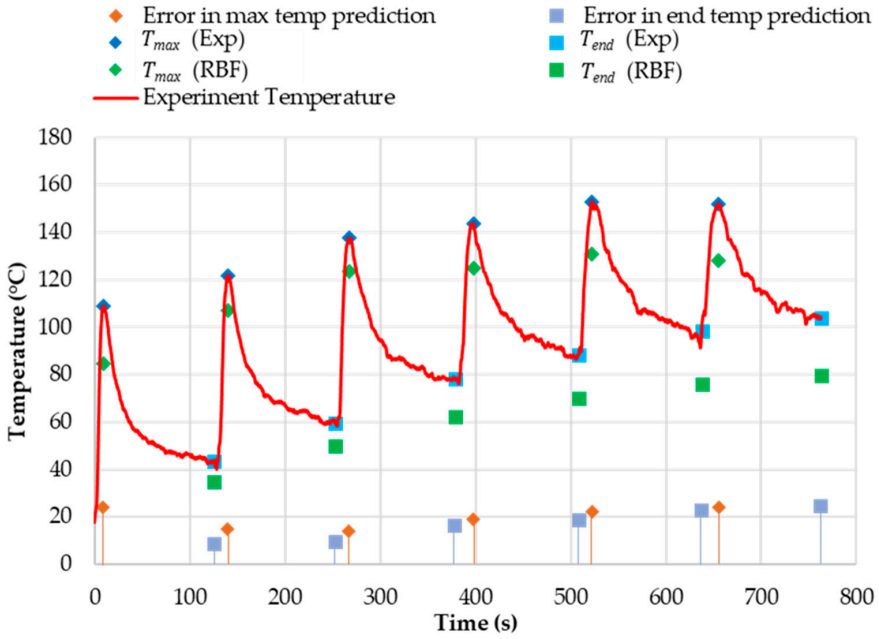

Figure 11. Comparison of T_{max} and T_{end} between RBF prediction and experimental data at location T1.

3.4.2. High-Fidelity Model

A comprehensive evaluation involved ten different ML models, with the aim to assess their performance across several metrics, such as MAE, mean squared error (MSE), root mean squared error (RMSE), R^2, and time. The results are shown in Table A4 of Appendix C. The models were trained on dataset D_{HFM}, obtained from the DOE simulation runs, which included parameters η, h, ε, and t, alongside temperature measurements to predict the overall temperature profile with high accuracy. The Extra Trees Regressor emerged as the preferred model, as the performance metrics were compelling, achieving an MSE of 1.1552 and an R^2 score of 0.99, demonstrating its superior predictive capabilities. To further validate the robustness of the Extra Trees Regressor, a 5-fold cross-validation was performed. The results are summarized in Table A5. The cross-validation results confirmed the reliability and consistency of the Extra Trees Regressor, with an average MSE of 0.520037 and an average R^2 score of 0.999715. The low variance in MSE across the folds indicates that the model generalized well to unseen data. The high R^2 scores across all folds underscored the model's capacity to explain nearly all the variance in the target variable. These findings suggest that the Extra Trees Regressor not only provided accurate predictions but also maintained stability and robustness across different subsets of the dataset. Thus, it was a highly reliable model for the calibration of the simulation process in this study.

3.5. Calibration of the Simulation Model

The calibration approach began with refining the parameter space using the LF model optimization. The best parameter set obtained from the LF model optimization was η = 0.64, h = 0.0000249, and ε = 0.99. Using this parameter set, a simulation was run to determine the temperature at the T1 location. For each layer, the maximum and end temperatures were recorded and compared with the LF model's predicted values. The observed error, shown in Figure 12, was expected because the LF model was based on a small dataset containing only the T_{max} and T_{end} for each layer. To improve the calibration accuracy, the parameter space surrounding the results predicted by the LF model optimization was explored through HF model optimization. This exploration was guided by Bayesian optimization to systematically identify the optimal parameter set. A graphical representation of how the parameter space was explored during the calibration process is shown in Figure 12.

The HF model optimization provided the final calibration parameters: η = 0.689, h = 0.0000186, and ε = 0.90. Further details of the Bayesian optimization can be found in Table A6. Following this optimization, a simulation was performed to obtain temperature data at the T1 location using these parameters. Figure 13 shows the comparison of experimental data and the simulation temperature at the T1 location. The visual plot supports the success of the calibration strategy, where the simulation model, after optimization, mirrored the experimental temperature profiles with impressive accuracy.

Also, in the same plot, the absolute error between these two datasets is shown. The MAE between experiment and simulation temperatures was 7.47 °C, indicating a strong alignment between the simulation and the experimental data throughout most of the deposition process. Notably, there were instances, particularly during the rapid temperature changes associated with layer deposition and the onset of dwell times, where the error spikes were observed. These occasional spikes, reaching up to 35 °C, may be attributed to the relatively short heating period (approximately 4–5 s), which limits the temporal resolution available for capturing the rapid thermal dynamics during the deposition process.

Despite these peaks, the overall error profile was consistent with the anticipated variability in a complex thermal system, such as W-DED. Despite these intermittent variances, the simulation showcased a high degree of precision. To extend the verification, temperatures at the T4 location were also extracted from the simulation for comparative analysis with the experimental data (Figure 14).

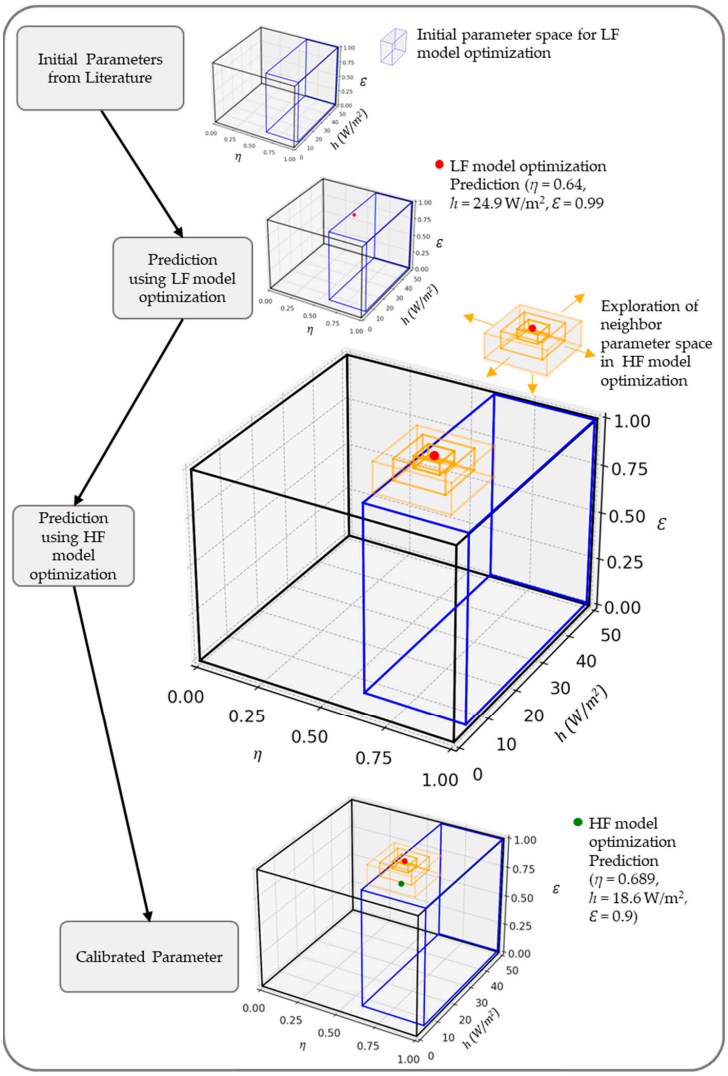

Figure 12. Visualization of parameter space updates during the calibration process.

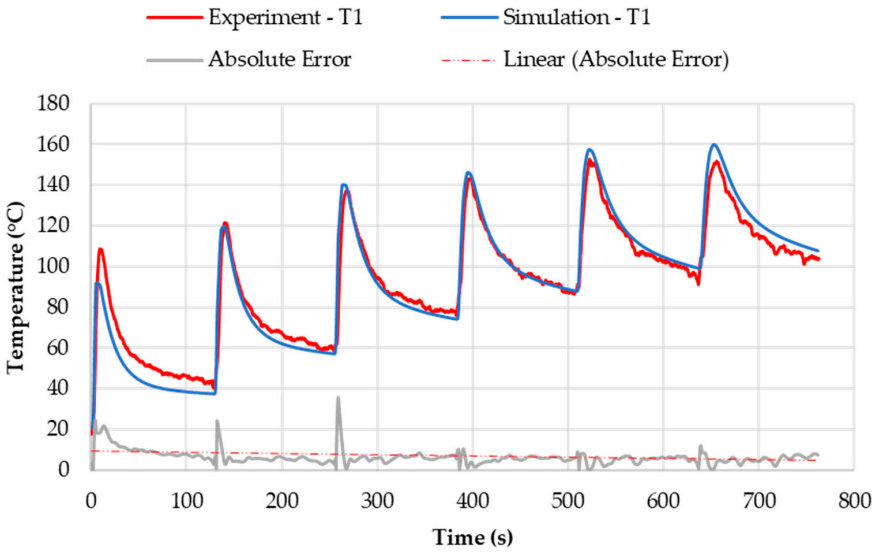

Figure 13. Absolute error between experimental and simulation temperatures (using calibrated parameters) at the T1 location.

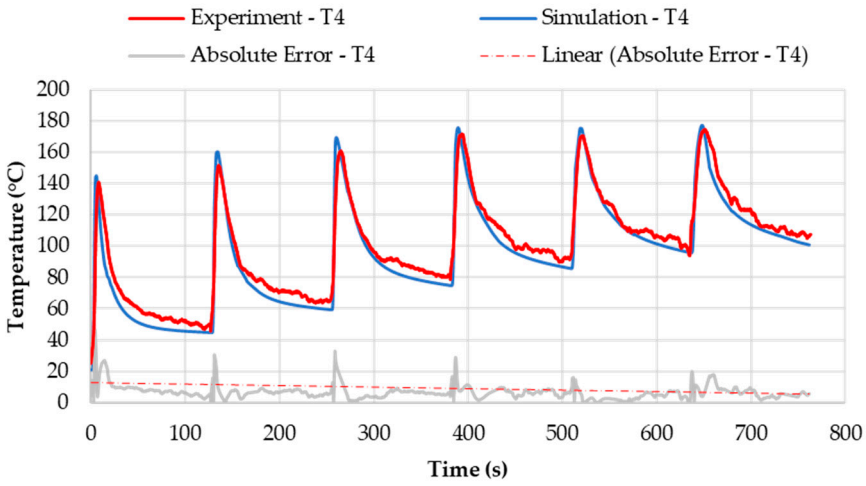

Figure 14. Comparison between experimental and simulation temperatures (using calibrated parameters) at the T4 location.

The MAE for the T4 location was 7.36 °C, which further supports the accuracy of the simulation in reflecting the experimental temperature profiles. Collectively, the outcomes of the multi-layer calibration confirmed the robustness and reliability of the calibration model. The calibrated simulation model demonstrated high precision in matching experimental temperature profiles, emphasizing its potential in refining the W-DED process simulations and enhancing predictive capabilities.

4. Conclusions and Future Work

This study successfully introduced a multi-fidelity modeling framework that significantly enhanced the calibration accuracy of thermal analysis in W-DED processes. By seamlessly integrating LF and HF models within a Bayesian optimization strategy, a comprehensive method was developed for aligning simulation outputs with experimental thermal data. The foundation of this approach was a structured DOE, which guided broad parameter exploration using the LF model and pinpointed likely areas for more detailed analysis. The HF model then conducted further optimization within the refined parameter space to identify the parameter set that produced an accurate and complete temperature profile. Key parameters optimized in this study included η, h, and ε, which are crucial for influencing the thermal behavior of the W-DED process and achieving an accurate match between simulation and experimental observations. The optimization process, driven by GP-based Bayesian optimization, balanced exploration and exploitation to minimize the MAE between experimental and simulation temperatures. This approach resulted in an MAE as low as 7.47 °C, validating the effectiveness of the strategy through multi-layer calibration. This modeling framework bridges the gap between numerical simulations and practical experimental observations, offering a systematic approach to fine-tuning the calibration in W-DED simulations. The methodology demonstrates the reliability of the simulation models and enhances trust in simulation-generated data for research and industrial applications, leading to more precise and reliable manufacturing outcomes.

Looking forward, future research should expand on this foundation to apply multi-fidelity models to more complex geometries and diverse materials, further advancing the precision of AM simulations. An important area for advancement could involve the dynamic adaptation of parameters such as emissivity, which may vary with temperature across different layers, to refine the model's responsiveness to real-world conditions. Ultimately, the application of this advanced modeling framework promises to streamline development cycles in W-DED by improving process reliability and product quality. It provides a replicable method that could significantly reduce the need for extensive experimental setups, ensuring manufacturing processes meet stringent quality requirements.

Supplementary Materials: The following supporting information can be downloaded at: https://www.mdpi.com/article/10.3390/jmmp8050222/s1, Supplmentary Data. DLFM Dataset for LF model. DHFM Dataset for HF model.

Author Contributions: Conceptualization, F.H. and A.H.; methodology, F.H. and A.H.; software, F.H. and A.H.; validation, F.H. and A.H.; formal analysis, F.H.; investigation, F.H. and M.M.R.; resources, T.D. and A.A.; data curation, F.H.; writing—original draft preparation, F.H.; writing—review and editing, A.H. and D.M.; visualization, F.H.; supervision, A.H. and D.M.; project administration, A.H., D.M. and A.A.; funding acquisition, A.A. All authors have read and agreed to the published version of the manuscript.

Funding: This research was funded by DEVCOM—Army Research Laboratory (ARL), grant number W911NF2020256.

Data Availability Statement: Data are unavailable due to privacy or ethical restrictions.

Acknowledgments: A. Agarwal, D. McDaniel, A. Hamrani, T. Dolmetsch, and M. M. Rayhan acknowledge the financial support of DEVCOM—Army Research Laboratory (ARL), grant number W911NF2020256.

Conflicts of Interest: The authors declare no conflicts of interest.

Abbreviation

AM	Additive manufacturing
BBD	Box–Behnken design
CCD	Central composite design
c	Specific heat capacity
DOE	Design of experiments
ε	Emissivity
FFD	Full factorial design
FEM	Finite element modeling
GP	Gaussian process
h	Convection film coefficient
HF	High fidelity
k	Thermal conductivity
LF	Low fidelity
MAE	Mean absolute error
MF	Multi-fidelity
MSE	Mean squared error
ρ	Density
RBF	Radial basis function
RMSE	Root mean squared error
RSM	Response surface model
T_{end}	Temperature at the end of dwell time
T_{max}	Maximum temperature
η	Thermal efficiency factor
W-DED	Wire-arc directed energy deposition
WAAM	Wire-arc additive manufacturing

Appendix A

Appendix A discusses parameter sensitivity analysis, comparison of design of experiment (DOE) methodologies, and DOE configurations. A parameter sensitivity analysis was conducted for the three parameters considered for calibrating the simulation model: η, h, and ε. Figure A1 presents the analysis within its feasible range, while holding the other two parameters at fixed baseline values. This analysis helped illustrate their individual influence on the temperature distribution. The results revealed that η significantly influenced T_{max} in each layer, emphasizing its role in heat generation and distribution within the substrate and deposited layers. The h and ε markedly affected the temperature profile during the cooling period, particularly in the later layers of the deposition process.

Overall, this analysis underscored the criticality of η, h, and ε, confirming their integral role in achieving an accurate thermal model for the W-DED process.

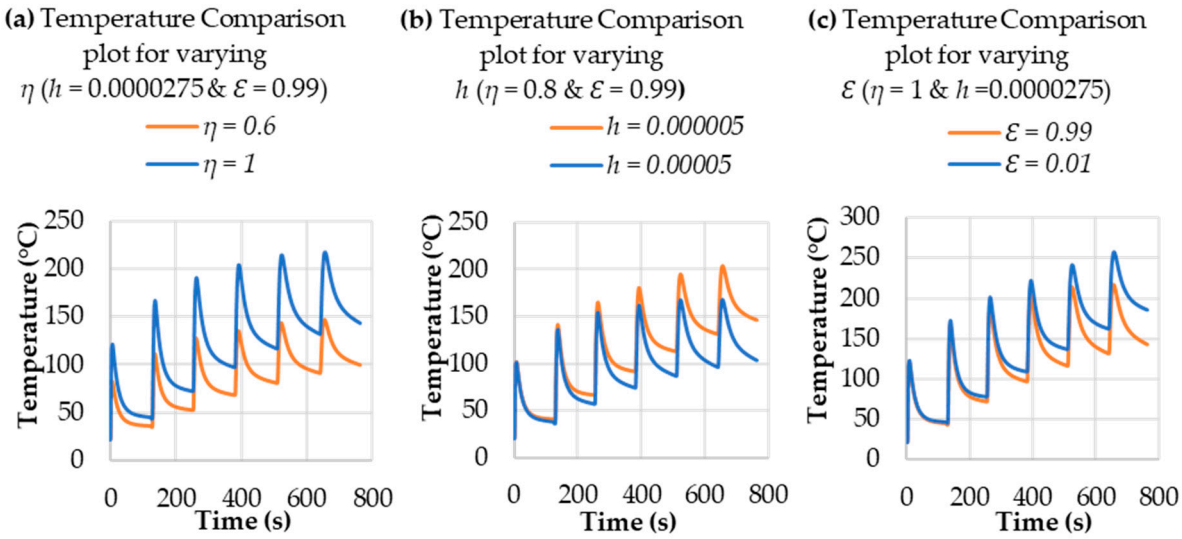

Figure A1. Parameter sensitivity analysis of the three parameters: (**a**) η, (**b**) h, and (**c**) ε.

A comparison of the DOE methodologies was conducted, and based on that, the Box–Behnken design (BBD) was selected. The DOE comparison and BBD simulation configuration are listed in Tables A1 and A2.

Table A1. Comparison of DOE methodologies and simulation requirements.

Name of DOE	No. of Simulations
Box–Behnken design	13
Central composite design	22
Full factorial design	27

Table A2. BBD simulation configurations.

No.	η	h (W/mm^2)	ε
1	0.6	0.000005	0.5
2	0.99	0.000005	0.5
3	0.6	0.00005	0.5
4	0.99	0.00005	0.5
5	0.6	0.0000275	0.01
6	0.99	0.0000275	0.01
7	0.6	0.0000275	0.99
8	0.99	0.0000275	0.99
9	0.8	0.000005	0.0.1
10	0.8	0.00005	0.01
11	0.8	0.000005	0.99
12	0.8	0.00005	0.99
13	0.8	0.0000275	0.5

Appendix B

Appendix B presents a comprehensive comparison of interpolation models that analyze thermal dynamics during material deposition processes. The models provide predictions for two crucial temperature points during each deposition layer: the maximum temperature (T_{max}), capturing the peak temperature of each layer, and the end temperature (T_{end}), observed after a designated dwell time. The comparison includes four interpolation methods: linear, polynomial, radial basis function (RBF), and kriging (Table A1). The visualizations illustrate the impact of calibration parameters, such as the thermal efficiency factor (η), convection film coefficient (h), and emissivity (ε), on T_{max} and T_{end}. Figures A2 and A3 display the evaluation results of all models for all 13 simulations in this study, showcasing a total of 12 models. The results are organized in a table format (Table A3), highlighting the mean squared error (MSE) and the coefficient of determination (R^2) for each model, providing a clear understanding of their performance across different layers.

Table A3. Comparison of interpolation models for maximum temperature and end temperature across different layers.

		Maximum Temperature		End Temperature	
Model	**Layer**	**MSE**	**R^2**	**MSE**	**R^2**
Linear	1	1.95785	0.99511	32.7835	0.00782
Linear	2	65	0.91579	168.981	0.02525
Linear	3	239.19	0.7785	471.389	0.05004
Linear	4	593.024	0.56174	934.328	0.11967
Linear	5	1084.38	0.37937	1517.54	0.16379
Linear	6	1691.16	0.2176	2157.58	0.19273
Polynomial	1	1.85112	0.99537	27.6582	0.16294
Polynomial	2	57.4989	0.92551	141.342	0.18469
Polynomial	3	203.992	0.8111	381.199	0.15087
Polynomial	4	485.343	0.64132	730.741	0.1243
Polynomial	5	856.403	0.50985	1159.62	0.1107
Polynomial	6	1298.76	0.39914	1622.45	0.1031
RBF	1	4.05×10^{-22}	1	3.1×10^{-21}	1
RBF	2	4.82×10^{-21}	1	1.9×10^{-20}	1
RBF	3	1.88×10^{-20}	1	3.5×10^{-20}	1
RBF	4	6.94×10^{-20}	1	2.9×10^{-20}	1
RBF	5	1.25×10^{-19}	1	6.2×10^{-20}	1
RBF	6	5.80×10^{-20}	1	1×10^{-19}	1
Kriging	1	inf	inf	12.8729	0.61041
Kriging	2	0.20831	0.99973	65.4305	0.62257
Kriging	3	0.68909	0.99936	180.618	0.59767
Kriging	4	1.98457	0.99853	358.342	0.57057
Kriging	5	371.739	0.78724	584.417	0.55182
Kriging	6	585.332	0.7292	827.623	0.54248

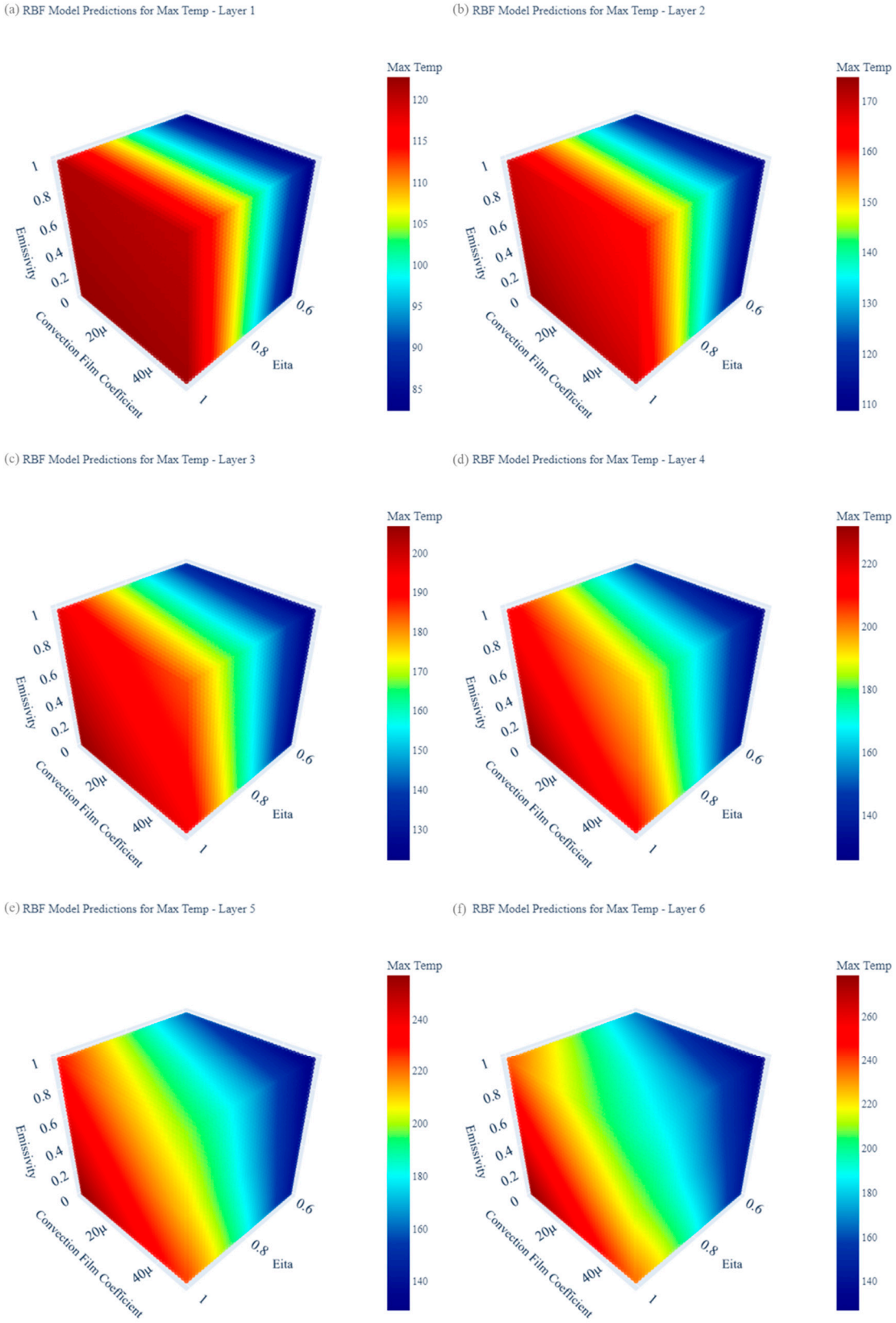

Figure A2. RBF model for all 6 layers for maximum temperature in a layer.

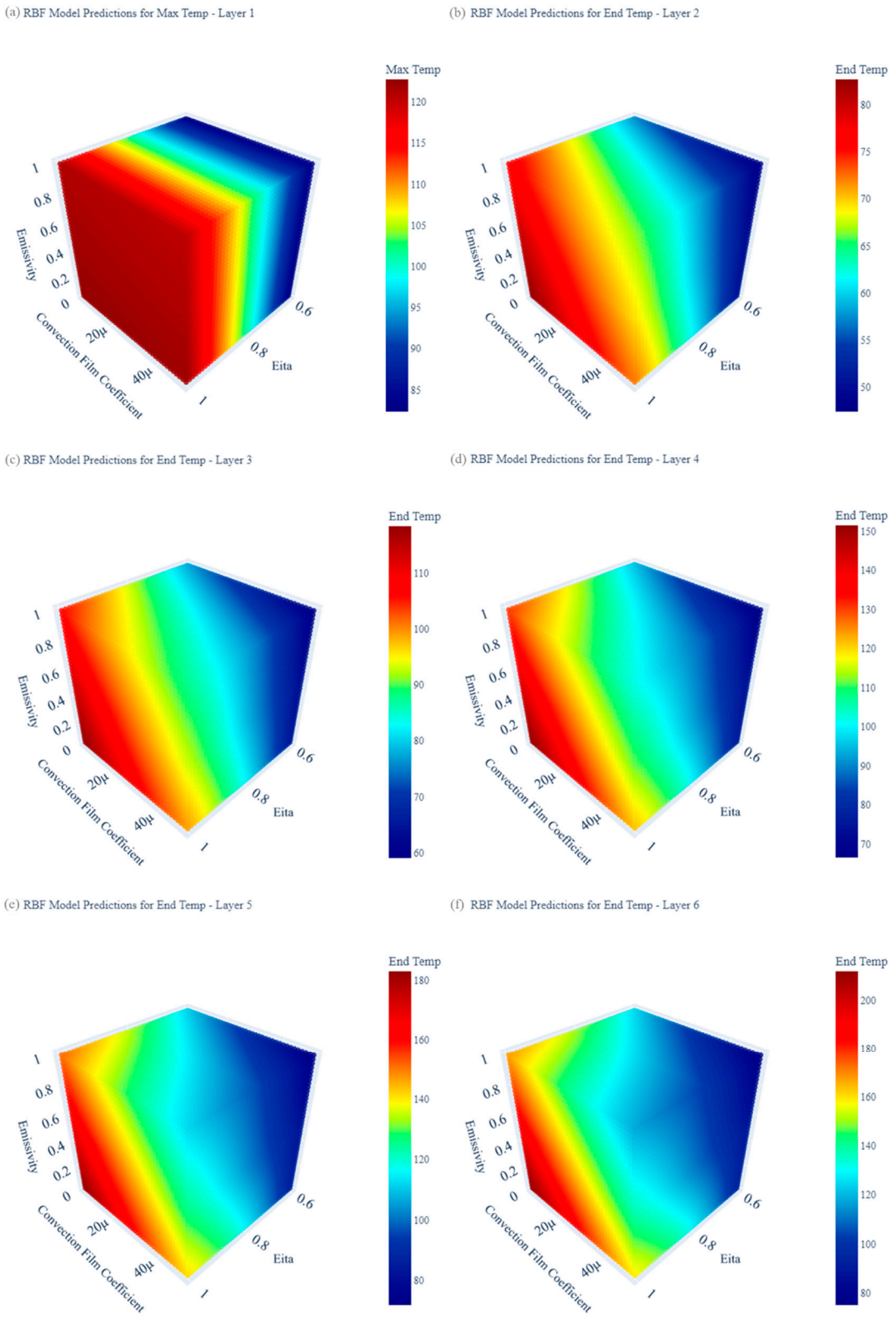

Figure A3. RBF model for all 6 layers for end temperature in a layer.

Appendix C

The comparative table for evaluating the best ML model and the cross-validation results of the selected model is listed in Tables A4 and A5, respectively.

Table A4. Comparative evaluation of ML models.

Model	MAE	MSE	RMSE	R^2	Time (s)
Extra Trees Regressor	0.3761	1.1552	1.0207	0.9999	0.157
Random Forest Regressor	1.365	8.4335	2.8785	0.9996	0.166
Light Gradient Boosting Machine	2.0142	14.2078	3.74	0.9993	0.838
Decision Tree Regressor	2.0984	22.8866	4.7295	0.9988	0.014
Gradient Boosting Regressor	9.1972	171.2841	13.0494	0.9912	0.096
AdaBoost Regressor	29.3596	1418.83	37.6006	0.9266	0.082
K Neighbors Regressor	30.6499	2066.029	45.3887	0.8931	0.281
Linear Regression	90.3094	14163.48	118.9368	0.2706	0.01
Least Angle Regression	90.3211	14162.43	118.9322	0.2706	0.009
Ridge Regression	92.3224	14625.5	120.8777	0.2466	0.009

Table A5. Cross-validation results of Extra Trees Regressor.

Fold	MSE	R^2
1	0.601965	0.999661
2	0.506924	0.999722
3	0.295647	0.999831
4	0.954419	0.999494
5	0.241231	0.999866
Average	0.520037	0.999715

Table A6. Summary of the Bayesian optimization process.

Parameters	Value
Callback function	DeltaYStopper
Stopping criteria	MAE improvement < 0.1 °C
No. of iterations when optimization stopped	43
Final combined MAE for all layers	74.03 °C
Calibrated parameters	η = 0.689, h = 0.0000186 W/mm^2, ε = 0.90

References

1. Taşdemir, A.; Nohut, S. An Overview of Wire Arc Additive Manufacturing (WAAM) in Shipbuilding Industry. *Ships Offshore Struct.* **2020**, *16*, 797–814. [CrossRef]
2. Busachi, A.; Erkoyuncu, J.; Colegrove, P.; Martina, F.; Ding, J. Designing a WAAM Based Manufacturing System for Defence Applications. *Procedia CIRP* **2015**, *37*, 48–53. [CrossRef]
3. Li, Y.; Su, C.; Zhu, J. Comprehensive Review of Wire Arc Additive Manufacturing: Hardware System, Physical Process, Monitoring, Property Characterization, Application and Future Prospects. *Results Eng.* **2022**, *13*, 100330. [CrossRef]
4. Montevecchi, F.; Venturini, G.; Grossi, N.; Scippa, A.; Campatelli, G. Finite Element Mesh Coarsening for Effective Distortion Prediction in Wire Arc Additive Manufacturing. *Addit. Manuf.* **2017**, *18*, 145–155. [CrossRef]
5. Gurmesa, F.D.; Lemu, H.G. Literature Review on Thermomechanical Modelling and Analysis of Residual Stress Effects in Wire Arc Additive Manufacturing. *Metals* **2023**, *13*, 526. [CrossRef]
6. Singh Sivam Sundarlingam Paramasivam, S.; Damodar Sawant, L.; Natarajan, H.; Sumanth, U.; Pratap Singh, K. Numerical Simulation Process Parameter Optimization in Metal Additive Manufacturing for Getting Better Quality of Products. *Mater. Today Proc.* **2022**, *66*, 850–857. [CrossRef]
7. Tröger, J.A.; Hartmann, S.; Treutler, K.; Potschka, A.; Wesling, V. Simulation-Based Process Parameter Optimization for Wire Arc Additive Manufacturing. *Prog. Addit. Manuf.* **2024**. [CrossRef]

8. Singh, C.P.; Sarma, R.; Kapil, S. The Qualitative Analysis of Warpage on Residual Stresses in Wire Arc Additive Manufacturing. *Mater Today Proc.* **2022**, *62*, 6619–6627. [CrossRef]
9. Huang, H.; Ma, N.; Chen, J.; Feng, Z.; Murakawa, H. Toward Large-Scale Simulation of Residual Stress and Distortion in Wire and Arc Additive Manufacturing. *Addit. Manuf.* **2020**, *34*, 101248. [CrossRef]
10. Li, R.; Wang, G.; Zhao, X.; Dai, F.; Huang, C.; Zhang, M.; Chen, X.; Song, H.; Zhang, H. Effect of Path Strategy on Residual Stress and Distortion in Laser and Cold Metal Transfer Hybrid Additive Manufacturing. *Addit. Manuf.* **2021**, *46*, 102203. [CrossRef]
11. Alhakeem, M.M.; Mollamahmutoglu, M.; Yilmaz, O.; Bol, N.; Kara, O.E. A Deposition Strategy for Wire Arc Additive Manufacturing Based on Temperature Variance Analysis to Minimize Overflow and Distortion. *J. Manuf. Process* **2023**, *85*, 1208–1220. [CrossRef]
12. Müller, J.; Hensel, J. Potential of Thermography for the Monitoring of DED-Arc Processes. *Weld. World* **2024**, *68*, 505–513. [CrossRef]
13. Goyal, R.; Johnson, E.; El-Zein, M.; Goldak, J.; Coulombe, M.; Tchernov, S. A Model Equation for the Convection Coefficient for Thermal Analysis of Welded Structures. In *ASM Proceedings of the International Conference: Trends in Welding Research*; ASM International: Novelty, OH, USA, 2009; pp. 321–327.
14. Dupont, J.N.; Marder, A.R. Thermal Efficiency of Arc Welding Processes. *Weld. J.* **1995**, *74*, 406–416.
15. Richter, A.; Gehling, T.; Treutler, K.; Wesling, V.; Rembe, C. Real-Time Measurement of Temperature and Volume of the Weld Pool in Wire-Arc Additive Manufacturing. *Meas. Sens.* **2021**, *17*, 100060. [CrossRef]
16. Zhao, X.F.; Zapata, A.; Zaeh, M.F. A Semi-Analytical Approach to Wire Arc Additive Manufacturing Simulation for Deposition Sequence Optimisation. *Virtual Phys. Prototyp.* **2024**, *19*, e2368648. [CrossRef]
17. Yang, J.; Kyvelou, P.; Wadee, M.A.; Gardner, L. Simulation and Prediction of Residual Stresses in WAAM-Strengthened I-Sections. *Structures* **2024**, *69*, 107248. [CrossRef]
18. Bai, X.; Zhang, H.; Wang, G. Improving Prediction Accuracy of Thermal Analysis for Weld-Based Additive Manufacturing by Calibrating Input Parameters Using IR Imaging. *Int. J. Adv. Manuf. Technol.* **2013**, *69*, 1087–1095. [CrossRef]
19. Chiumenti, M.; Lin, X.; Cervera, M.; Lei, W.; Zheng, Y.; Huang, W. Numerical Simulation and Experimental Calibration of Additive Manufacturing by Blown Powder Technology. Part I: Thermal Analysis. *Rapid Prototyp. J.* **2017**, *23*, 448–463. [CrossRef]
20. Mahmoudi, M.; Tapia, G.; Karayagiz, K.; Franco, B.; Ma, J.; Arroyave, R.; Karaman, I.; Elwany, A. Multivariate Calibration and Experimental Validation of a 3D Finite Element Thermal Model for Laser Powder Bed Fusion Metal Additive Manufacturing. *Integr. Mater. Manuf. Innov.* **2018**, *7*, 116–135. [CrossRef]
21. He, F.; Yuan, L.; Mu, H.; Ros, M.; Ding, D.; Pan, Z.; Li, H. Research and Application of Artificial Intelligence Techniques for Wire Arc Additive Manufacturing: A State-of-the-Art Review. *Robot. Comput. Integr. Manuf.* **2023**, *82*, 102525. [CrossRef]
22. Mu, H.; He, F.; Yuan, L.; Commins, P.; Wang, H.; Pan, Z. Toward a Smart Wire Arc Additive Manufacturing System: A Review on Current Developments and a Framework of Digital Twin. *J. Manuf. Syst.* **2023**, *67*, 174–189. [CrossRef]
23. Hamrani, A.; Agarwal, A.; Allouhi, A.; McDaniel, D. Applying Machine Learning to Wire Arc Additive Manufacturing: A Systematic Data-Driven Literature Review. *J. Intell. Manuf.* **2023**, *35*, 2407–2439. [CrossRef]
24. Gunasegaram, D.R.; Murphy, A.B.; Barnard, A.; DebRoy, T.; Matthews, M.J.; Ladani, L.; Gu, D. Towards Developing Multiscale-Multiphysics Models and Their Surrogates for Digital Twins of Metal Additive Manufacturing. *Addit. Manuf.* **2021**, *46*, 102089. [CrossRef]
25. Xia, C.; Pan, Z.; Polden, J.; Li, H.; Xu, Y.; Chen, S. Modelling and Prediction of Surface Roughness in Wire Arc Additive Manufacturing Using Machine Learning. *J. Intell. Manuf.* **2021**, *33*, 1467–1482. [CrossRef]
26. Strobl, D.; Unger, J.F.; Ghnatios, C.; Klawonn, A.; Pittner, A.; Rethmeier, M.; Robens-Radermacher, A. Efficient Bead-on-Plate Weld Model for Parameter Estimation towards Effective Wire Arc Additive Manufacturing Simulation. *Weld. World* **2024**, *68*, 969–986. [CrossRef]
27. Knapp, G.L.; Coleman, J.; Rolchigo, M.; Stoyanov, M.; Plotkowski, A. Calibrating Uncertain Parameters in Melt Pool Simulations of Additive Manufacturing. *Comput. Mater. Sci.* **2023**, *218*, 111904. [CrossRef]
28. Olleak, A.; Xi, Z. Calibration and Validation Framework for Selective Laser Melting Process Based on Multi-Fidelity Models and Limited Experiment Data. *J. Mech. Des.* **2020**, *142*, 081701. [CrossRef]
29. Oleynik, M.; Balyakin, A.; Khaimovich, A.; Zlobin, E. Development of a Calibration Technique of a Finite Element Model for Calculating Compensation of Deformations from the Action of Residual Stresses in Additive Manufacturing. *E3S Web Conf.* **2023**, *458*, 02023. [CrossRef]
30. Park, E.G.; Kang, J.W.; Cho, J.Y.; Kim, J.H. Calibration Technique of Thermal Analysis Model for Metal Additive Manufacturing Process Simulation by Nonlinear Regression and Optimization. *Appl. Sci.* **2021**, *11*, 1647. [CrossRef]
31. Feng, G.; Wang, H.; Wang, Y.; Deng, D.; Zhang, J. Numerical Simulation of Residual Stress and Deformation in Wire Arc Additive Manufacturing. *Crystals* **2022**, *12*, 803. [CrossRef]
32. Goldak, J.; Chakravarti, A.; Bibby, M. A New Finite Element Model for Welding Heat Sources. *Metall. Trans. B* **1984**, *15*, 299–305. [CrossRef]
33. Giarollo, D.F.; Mazzaferro, C.C.P.; Mazzaferro, J.A.E. Comparison between Two Heat Source Models for Wire-Arc Additive Manufacturing Using GMAW Process. *J. Braz. Soc. Mech. Sci. Eng.* **2022**, *44*, 7. [CrossRef]
34. Planck, M. *The Theory of Heat Radiation*; P. Blakiston, Son & Co.: Philadelphia, PA, USA, 2012.

35. Graf, M.; Hälsig, A.; Höfer, K.; Awiszus, B.; Mayr, P. Thermo-Mechanical Modelling of Wire-Arc Additive Manufacturing (WAAM) of Semi-Finished Products. *Metals* **2018**, *8*, 1009. [CrossRef]
36. Arshad, H.M.; Akhtar, M.; Gilmour, S.G. Augmented Box-Behnken Designs for Fitting Third-Order Response Surfaces. *Commun. Stat. Theory Methods* **2012**, *41*, 4225–4239. [CrossRef]
37. Fasshauer, G.E. *Meshfree Approximation Methods with MATLAB*; World Scientific: Singapore, 2007; ISBN 9789812706331.
38. Hamrani, A.; Belaidi, I.; Bouarab, Z. A Smoothed Radial Point Interpolation Method (S-RPIM) for Large-Deformation Elasto-Visco-Plastic Analysis Occurring in Sheet Metal Blanking Processes. In *CFM 2017-23ème Congrès Français de Mécanique*; AFM, Maison de la Mécanique: Courbevoie, France, 2017.
39. Hamrani, A.; Belaidi, I.; Monteiro, E.; Lorong, P. On the Factors Affecting the Accuracy and Robustness of Smoothed-Radial Point Interpolation Method. *Adv. Appl. Math. Mech.* **2017**, *9*, 43–72. [CrossRef]
40. Matérn, B. *Spatial Variation: Stochastic Models and Their Application to Some Problems in Forest Surveys and Other Sampling Investigations*; Statens Skogsforskningsinstitut: Stockholm, Sweden, 1960; pp. 1–140.
41. Rasmussen, C.E.; Williams, C.K.I. *Gaussian Processes for Machine Learning*; MIT Press: Cambridge, MA, USA, 2006; ISBN 026218253X.
42. Jones, D.R.; Schonlau, M.; Welch, W.J. Efficient Global Optimization of Expensive Black-Box Functions. *J. Glob. Optim.* **1998**, *13*, 455–492. [CrossRef]
43. Montevecchi, F.; Venturini, G.; Scippa, A.; Campatelli, G. Finite Element Modelling of Wire-Arc-Additive-Manufacturing Process. *Procedia CIRP* **2016**, *55*, 109–114. [CrossRef]
44. Zhang, L.; Michaleris, P. Investigation of Lagrangian and Eulerian Finite Element Methods for Modeling the Laser Forming Process. *Finite Elem. Anal. Des.* **2004**, *40*, 383–405. [CrossRef]
45. Le, V.T.; Bui, M.C.; Pham, T.Q.D.; Tran, H.S.; Van Tran, X. Efficient Prediction of Thermal History in Wire and Arc Additive Manufacturing Combining Machine Learning and Numerical Simulation. *Int. J. Adv. Manuf. Technol.* **2023**, *126*, 4651–4663. [CrossRef]
46. Reimann, J.; Hammer, S.; Henckell, P.; Rohe, M.; Ali, Y.; Rauch, A.; Hildebrand, J.; Bergmann, J.P. Directed Energy Deposition-Arc (Ded-Arc) and Numerical Welding Simulation as a Hybrid Data Source for Future Machine Learning Applications. *Appl. Sci.* **2021**, *11*, 7075. [CrossRef]
47. Venkata Rao, K.; Parimi, S.; Suvarna Raju, L.; Suresh, G. Modelling and Optimization of Weld Bead Geometry in Robotic Gas Metal Arc-Based Additive Manufacturing Using Machine Learning, Finite-Element Modelling and Graph Theory and Matrix Approach. *Soft Comput.* **2022**, *26*, 3385–3399. [CrossRef]
48. Ma, C.; Li, C.; Yan, Y.; Liu, Y.; Wu, X.; Li, D.; Han, Y.; Jin, H.; Zhang, F. Investigation of the In-Situ Gas Cooling of Carbon Steel during Wire and Arc Additive Manufacturing. *J. Manuf. Process* **2021**, *67*, 461–477. [CrossRef]
49. Bauer, A.; Scharf, R.; Hälsig, A.; Awiszus, B. Numerical Simulation and Calibration of a Single Seam WAAM Process with a Commercial and an Open Source Software. *J. Appl. Eng. Des. Simul.* **2021**, *1*, 25–31. [CrossRef]
50. Springer, S.; Röcklinger, A.; Leitner, M.; Grün, F.; Gruber, T.; Lasnik, M.; Oberwinkler, B. Implementation of a Viscoplastic Substrate Creep Model in the Thermomechanical Simulation of the WAAM Process. *Weld. World* **2022**, *66*, 441–453. [CrossRef]
51. Ding, J.; Colegrove, P.; Mehnen, J.; Ganguly, S.; Almeida, P.M.S.; Wang, F.; Williams, S. Thermo-Mechanical Analysis of Wire and Arc Additive Layer Manufacturing Process on Large Multi-Layer Parts. *Comput Mater Sci* **2011**, *50*, 3315–3322. [CrossRef]
52. Bai, X.; Colegrove, P.; Ding, J.; Zhou, X.; Diao, C.; Bridgeman, P.; Roman Hönnige, J.; Zhang, H.; Williams, S. Numerical Analysis of Heat Transfer and Fluid Flow in Multilayer Deposition of PAW-Based Wire and Arc Additive Manufacturing. *Int. J. Heat Mass Transf.* **2018**, *124*, 504–516. [CrossRef]
53. Lu, X.; Lin, X.; Chiumenti, M.; Cervera, M.; Hu, Y.; Ji, X.; Ma, L.; Huang, W. In Situ Measurements and Thermo-Mechanical Simulation of Ti–6Al–4V Laser Solid Forming Processes. *Int. J. Mech. Sci.* **2019**, *153–154*, 119–130. [CrossRef]
54. Nijhuis, B.; Geijselaers, H.J.M.; van den Boogaard, A.H. Efficient Thermal Simulation of Large-Scale Metal Additive Manufacturing Using Hot Element Addition. *Comput. Struct.* **2021**, *245*, 106463. [CrossRef]
55. Sandeep, K.J.; Teja, P.J.; Choudhary, A.K.; Jain, R. Development of Correlation between Temperature, Liquid Life Span, Molten Pool, and Porosity during Wire Arc Additive Manufacturing: A Finite Element Approach. *CIRP J. Manuf. Sci. Technol.* **2022**, *38*, 274–287. [CrossRef]